EUROPEAN ORGANIZATION FOR NUCLEAR RESEARCH (CERN)

CERN-PH-EP-2015-308
LHCb-PAPER-2015-040
December 1, 2015

Measurements of long-range near-side angular correlations in $\sqrt{s_{NN}} = 5\,\text{TeV}$ proton-lead collisions in the forward region

The LHCb collaboration[†]

Abstract

Two-particle angular correlations are studied in proton-lead collisions at a nucleon-nucleon centre-of-mass energy of $\sqrt{s_{NN}} = 5\,\text{TeV}$, collected with the LHCb detector at the LHC. The analysis is based on data recorded in two beam configurations, in which either the direction of the proton or that of the lead ion is analysed. The correlations are measured as a function of relative pseudorapidity, $\Delta\eta$, and relative azimuthal angle, $\Delta\phi$, for events in different classes of event activity and for different bins of particle transverse momentum. In high-activity events a long-range correlation on the near side, $\Delta\phi \approx 0$, is observed in the pseudorapidity range $2.0 < \eta < 4.9$. This measurement of long-range correlations on the near side in proton-lead collisions extends previous observations into the forward region up to $\eta = 4.9$. The correlation increases with growing event activity and is found to be more pronounced in the direction of the lead beam. However, the correlation strengths in the direction of the lead and proton beams are found to be compatible when comparing events with similar absolute activity in the direction analysed.

Submitted to Phys. Lett. B

[†]Authors are listed at the end of this paper.

1 Introduction

Studies of two-particle angular correlations are an important experimental method to investigate QCD effects in particle production and to probe collective effects arising in the dense environment of a high-energy collision. The highest particle densities and multiplicities reached in proton-proton (pp) and proton-lead collisions (pPb) at the LHC are of a similar size to those in non-central nucleus-nucleus (AA) collisions. This motivates looking for signatures which were so far mainly studied in AA collisions.

Two-particle correlations are conveniently described by two-dimensional $(\Delta\eta, \Delta\phi)$-correlation functions. For pairs of prompt charged particles their separations in pseudorapidity, $\Delta\eta$, and in the azimuthal angle, $\Delta\phi$, are measured. Structures in the correlation function are classified into short-range ($|\Delta\eta| \lesssim 2$) and long-range ($|\Delta\eta| \gtrsim 2$) effects. On the near-side ($|\Delta\phi| \approx 0$) a short-range correlation, the so-called "jet peak", is the dominant structure, caused by the fact that in the fragmentation process the final-state particles are collimated around the initial parton. To balance the momentum, the peak is accompanied by a long-range structure on the away side ($|\Delta\phi| \approx \pi$) caused by particles that are opposite in azimuthal angle.

Due to the different momentum fractions carried by the colliding partons and the resulting individual boosts, the away-side structure is not restricted in $\Delta\eta$, but elongated over a large range. In complex heavy-ion collisions, these short- and long-range structures are modified as a result of the strongly interacting medium that is formed depending on the centrality of the collision. Long-range correlations on the near- and away-side are observed, which are typically explained as being the result of a hydrodynamical flow of the deconfined medium [1]. Measurements in very rare pp collisions that have an extremely high particle multiplicity revealed a similar unexpected long-range correlation on the near side [2]. This structure, often referred to as the near-side "ridge", has also been confirmed in high-multiplicity pPb collisions [3–7], where it was found to be much more pronounced than in pp collisions.

The theoretical interpretation of the mechanism responsible for the ridge in pp and pPb is still under discussion. Various models have been proposed which include colour reconnection and gluon saturation in the framework of a colour-glass condensate [8–12], multiparton interactions [13–15], jet-medium interactions [16,17], and collective effects [18–21] induced by the formation and expansion of a high-density system possibly produced in these collisions.

Analyses that have seen the near-side ridge at the LHC have been performed in the central rapidity region, probing ranges up to $|\eta| = 2.5$. In a recent analysis [7] larger pseudorapidities were also accessed in measurements of correlations between particles produced in the forward ($2.5 < |\eta| < 4.0$) and in the central ($|\eta| < 1.0$) regions. For the present measurement the forward acceptance of the LHCb detector, unique among the LHC experiments, is used to study the ridge phenomenon in pPb collisions. Proton-lead collisions are analysed in the range of $2.0 < \eta < 4.9$ and in the directions of the proton and the lead beams separately. Confirmation of the ridge correlation at large pseudorapidities and comparison of its magnitude for the two beam directions provide new input to the

theoretical understanding of the underlying mechanisms.

2 Experimental setup

The analysis is based on data collected with the LHCb detector during the proton-lead data-taking period in 2013. The LHC provided pPb collisions at a nucleon-nucleon centre-of-mass energy of $\sqrt{s_{NN}} = 5\,\text{TeV}$, corresponding to a proton beam energy of 4 TeV and a lead beam energy of 1.58 TeV per nucleon. Due to this asymmetric beam configuration, there is a relative boost between the rapidity in the LHCb laboratory frame, y_{lab}, and y in the nucleon-nucleon centre-of-mass frame, corresponding to a shift of 0.47 units.

The LHCb detector [22, 23] is a single-arm forward spectrometer covering the pseudorapidity range $2 < \eta < 5$. Depending on the direction of the proton and the lead beam, two different configurations are distinguished. In the *forward* configuration the proton beam points to positive rapidity, into the LHCb spectrometer, and the recorded collisions are referred to as p+Pb. The opposite *backward* configuration, in which the lead beam points to positive rapidity, is referred to as Pb+p. The measurement is performed in the LHCb laboratory frame, probing rapidities y in the nucleon-nucleon centre-of-mass frame of $1.5 < y < 4.4$ in the p+Pb configuration and $-5.4 < y < -2.5$ in the Pb+p configuration. The data used for this analysis correspond to an integrated luminosity of $0.46\,\text{nb}^{-1}$ in the p+Pb configuration and $0.30\,\text{nb}^{-1}$ for the Pb+p configuration.

The LHCb detector, designed for the study of particles containing b or c quarks, includes a high-precision tracking system consisting of a silicon-strip vertex detector (VELO) surrounding the interaction region, a large-area silicon-strip detector located upstream of a dipole magnet with a bending power of about 4 Tm, and three stations of silicon-strip detectors and straw drift tubes placed downstream of the magnet. The polarity of the dipole magnet was reversed once for each configuration to average over small asymmetries in the detection of charged particles. The tracking system provides a measurement of momentum of charged particles with a relative uncertainty that varies from 0.5% at low momentum to 1.0% at 200 GeV/c. Different types of charged hadrons are distinguished using information from two ring-imaging Cherenkov detectors. Photons, electrons and hadrons are identified by a calorimeter system consisting of scintillating-pad and preshower detectors, an electromagnetic calorimeter and a hadronic calorimeter. Muons are identified by a system composed of alternating layers of iron and multiwire proportional chambers. The online event selection is performed by a trigger, which consists of a hardware stage, based on information from the calorimeter and muon systems, followed by a software stage, which applies a full event reconstruction. During data taking of pPb collisions, an activity trigger in the hardware stage accepted non-empty beam bunch crossings, and the software stage accepted events with at least one reconstructed track in the VELO.

3 Data selection and corrections

Monte Carlo simulations are used to evaluate the efficiency of the following selections and to estimate the remaining contamination in the selected track sample. Proton-lead collisions in p+Pb and Pb+p configurations are simulated using the HIJING generator [24]. As a cross-check, proton-proton collisions at a centre-of-mass energy of 8 TeV are simulated using PYTHIA [25] in a special LHCb configuration [26] and with a high average interaction rate (large pile-up) to reproduce the larger particle multiplicity in proton-lead collisions. Particle decays are simulated by EVTGEN [27]. The interaction of the generated particles with the detector, and its response, are implemented using the GEANT4 toolkit [28] as described in Ref. [29].

The measurements are based on proton-lead collisions that are dominated by single interactions; fewer than 2% of the bunch crossings have more than one interaction. Each event is required to have exactly one reconstructed primary vertex containing at least five tracks. Beam-related background interactions are suppressed by requiring the position of the reconstructed primary vertex to be within ± 3 standard deviations around the mean interaction point, separately for each coordinate. The mean value and the width of this luminous region are determined separately from a Gaussian fit to the distribution of reconstructed primary vertices of each data sample. Depending on the polarity of the magnetic field and the resulting beam optics, the size of the standard deviation along the beam axis is approximately 40 mm or 60 mm, while in the transverse direction it is around 30 μm. While pPb interactions are most likely produced in this region, beam-related background extends further along the beam line. Beam gas events or interactions with detector material can produce a very high number of particles; however, in such cases the total energy deposit in the calorimeter is much smaller than that of typical pPb collisions. Events with too small a ratio of the number of clusters in the electromagnetic calorimeter to that in the VELO are rejected; individual lower bounds are defined for collisions in the p+Pb and Pb+p configuration using simulation.

The angular correlations are determined for charged particles that are directly produced in the pPb interaction. The measurement is based on tracks traversing the full tracking system, which restricts charged particles in pseudorapidity to $2.0 < \eta < 4.9$. In addition, particles are required to have a transverse momentum $p_{\mathrm{T}} > 0.15\,\mathrm{GeV}/c$ and a total momentum $p > 2\,\mathrm{GeV}/c$. Reconstruction artefacts, such as fake tracks, are suppressed using a multivariate classifier. The remaining average fraction of fake tracks is of the order of 7% and 12% in the p+Pb and Pb+p samples, respectively. The probability of reconstructing fake tracks increases with the number of hits in the tracking detectors. Thus, the difference between the data samples is due to the higher average particle and hit multiplicity that is present in the direction of the lead remnant. To select primary tracks originating directly from the pPb collision the impact parameter of each track with respect to the reconstructed primary vertex must not exceed 1.2 mm, after which the fraction of remaining tracks from secondary particles is estimated to be less than 3.5%.

The inefficiency in finding charged particles arises from two effects: limited detector acceptance in the range of $2.0 < \eta < 4.9$, and limitations of the track reconstruction. For

particles fulfilling the kinematic requirements, the acceptance describes the fraction that reach the end of the downstream tracking stations. This multiplicity-independent efficiency is about 70% on average. In contrast, the track reconstruction efficiency varies from 96% for low-multiplicity events to 60% for events with the highest measured multiplicity.

After applying the selection requirements, the remaining probabilities of selecting fake tracks, $\mathcal{P}_{\text{fake}}$, and secondary particles, $\mathcal{P}_{\text{sec}}$, as well as the efficiencies related to the detector acceptance, ϵ_{acc}, and the track reconstruction, ϵ_{tr}, are estimated in simulation as a function of the angular variables η and ϕ, the transverse momentum p_{T}, and the hit-multiplicity in the VELO, $\mathcal{N}^{\text{hit}}_{\text{VELO}}$. Each reconstructed track is assigned a weight, ω, that accounts for these effects:

$$\omega(\eta, \phi, p_{\text{T}}, \mathcal{N}^{\text{hit}}_{\text{VELO}}) = (1 - \mathcal{P}_{\text{fake}} - \mathcal{P}_{\text{sec}})/(\epsilon_{\text{acc}} \cdot \epsilon_{\text{tr}}). \quad (1)$$

4 Activity classes and data samples

Two-particle correlations show a strong dependence on the number of particles produced within a collision. The hit multiplicity in the VELO is proportional to this global event property. With its coverage in pseudorapidity ranging from $1.9 < \eta < 4.9$ in the forward direction and $-2.5 < \eta < -2.0$ in the backward direction, the VELO can probe the total number of charged particles per event more comprehensively than other sub-detectors of LHCb.

Both p+Pb and Pb+p data samples consist of sub-samples, two minimum-bias and two high-multiplicity samples. The minimum-bias samples consist of about 1.1×10^8 events which are randomly selected from the full event samples. The high-multiplicity samples contain all events with at least 2200 hits in the VELO and amount to about 1.1×10^8 and 1.3×10^8 events in the p+Pb and Pb+p configurations, respectively.

Five event-activity classes are defined as fractions of the hit-multiplicity distributions of the minimum-bias samples, as indicated in Fig. 1. Since collisions recorded in the Pb+p configuration reach larger hit-multiplicities compared to those in the p+Pb configuration, the relative classes are defined separately for each configuration. The $50 - 100\%$ class contains approximately the 50% of events with the lowest event activities, followed by the $30 - 50\%$ and $10 - 30\%$ classes representing medium-activity events, and the $0 - 10\%$ and $0 - 3\%$ classes of high-activity events. The ranges defining the activity classes are listed in Table 1. For each class, average numbers of charged particles, $\langle N_{ch} \rangle_{\text{MC}}$, are quoted for illustration, based on the HIJING event generator.

The activity dependences of the long-range correlations in the direction of the fragmenting proton (p+Pb configuration) are compared to those in the direction of the fragmenting lead ion (Pb+p configuration). For this purpose, common absolute activity ranges for both beam configurations are studied, which only account for the particle production in the forward pseudorapidity range of $2.0 < \eta < 4.9$. The fraction of VELO hits related to the absolute activity in the acceptance $2.0 < \eta < 4.9$ is different in the p+Pb and Pb+p configurations. To account for this, in the definition of common absolute activity classes a scaling factor is applied to the hit multiplicities observed in the p+Pb configuration.

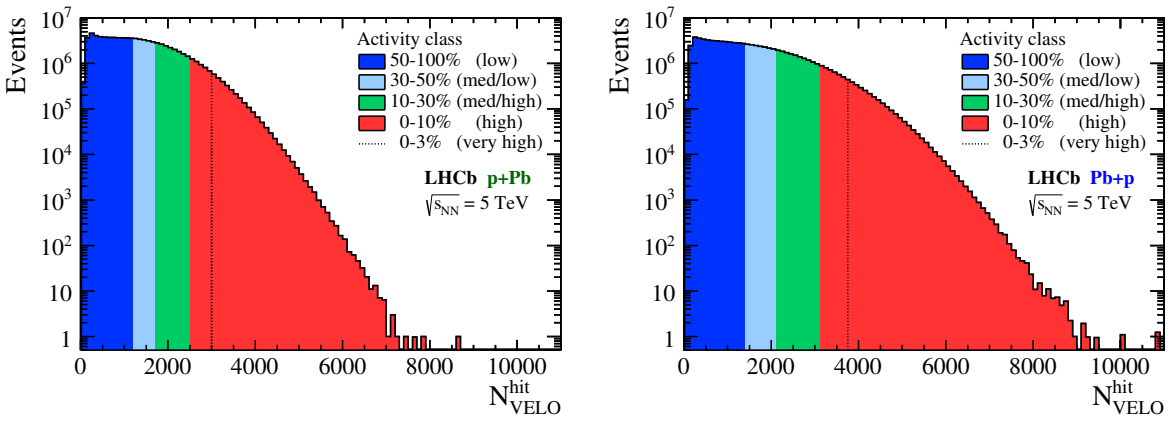

Figure 1: Hit-multiplicity distribution in the VELO for selected events of the minimum-bias samples in the (left) p+Pb and (right) Pb+p configurations. The activity classes are defined as fractions of the full distribution, as indicated by colours (shades). The $0-3\%$ class is a sub-sample of the $0-10\%$ class.

This scaling factor is determined to be 0.77 ± 0.08 by using the relation between hit and track multiplicities in the two beam configurations. The uncertainty accounts for deviations from perfect linearity in the data that are not reproduced in the simulation, and is propagated into the systematic uncertainties of the results. Five common absolute activity classes, labelled I – V, are defined in the high-activity region and are listed in Table 2 with the corresponding average numbers of charged particles from simulation. The quoted uncertainties in the p+Pb sample are related to the systematic uncertainty of the

Table 1: Relative event-activity classes defined by the VELO-hit multiplicity, $\mathcal{N}^{\rm hit}_{\rm VELO}$, of an event. The classes are defined as fractions of the $\mathcal{N}^{\rm hit}_{\rm VELO}$distribution for minimum-bias recorded events in the p+Pb or Pb+p configuration. The $0-3\%$ class is a sub-sample of the $0-10\%$ class. For illustration purposes the average number, $\langle N_{ch}\rangle_{\rm MC}$, of prompt charged particles with $p > 2\,\text{GeV}/c$, $p_{\rm T} > 0.15\,\text{GeV}/c$ and $2.0 < \eta < 4.9$ is listed for events simulated with the HIJING event generator. Statistical uncertainties are negligible.

Relative activity class		p+Pb range $\mathcal{N}^{\rm hit}_{\rm VELO}$	p+Pb $\langle N_{ch}\rangle_{\rm MC}$	Pb+p range $\mathcal{N}^{\rm hit}_{\rm VELO}$	Pb+p $\langle N_{ch}\rangle_{\rm MC}$
$50-100\%$	very low	$0-1200$	18.9	$0-1350$	29.2
$30-50\%$	low	$1200-1700$	30.0	$1350-2000$	47.4
$10-30\%$	medium	$1700-2400$	42.8	$2000-3000$	70.9
$0-10\%$	high	$2400-$ max	63.6	$3000-$ max	106.7
$0-3\%$	very high	$3000-$ max	73.7	$3800-$ max	126.4

Table 2: Common absolute activity bins for the p+Pb and Pb+p samples. The activity of p+Pb events is scaled to match the same activity ranges of Pb+p events, as explained in the text. For illustration purposes the average number, $\langle N_{ch}\rangle_{\rm MC}$, of prompt charged particles with $p > 2\,\text{GeV}/c$, $p_{\rm T} > 0.15\,\text{GeV}/c$ and $2.0 < \eta < 4.9$ is listed for events simulated with the HIJING event generator. The uncertainties are due to the scaling factor of 0.77 ± 0.08. Statistical uncertainties are negligible.

Common absolute activity bin	$\mathcal{N}^{\rm hit}_{\rm VELO}$-range in Pb+$p$ scale	p+Pb $\langle N_{ch}\rangle_{\rm MC}$	Pb+p $\langle N_{ch}\rangle_{\rm MC}$
Bin I	$2200 - 2400$	62.8 ± 6.6	64.4
Bin II	$2400 - 2600$	68.4 ± 7.1	67.0
Bin III	$2600 - 2800$	73.7 ± 7.6	76.4
Bin IV	$2800 - 3000$	79.2 ± 7.9	82.4
Bin V	$3000 - 3500$	86.7 ± 8.2	92.9

scaling factor.

The analysis is repeated using an alternative event-activity classification, based on the multiplicity of selected tracks (Sect. 3) in the range $2.0 < \eta < 4.9$. In analogy to the nominal approach using the VELO-hit multiplicity, the same fractions of the full distribution are used to define relative activity classes for both beam configurations. Similarly, five common activity bins for the p+Pb and Pb+p samples are defined in the intermediate to high-activity classes. The results are found to be independent of the definition of the activity classes.

5 Analysis method

Two-particle correlations are measured separately for events in each activity class. The track sample containing the selected candidates of primary charged particles is divided into three $p_{\rm T}$ intervals: $0.15 - 1.0\,\text{GeV}/c$, $1.0 - 2.0\,\text{GeV}/c$ and $2.0 - 3.0\,\text{GeV}/c$. For each event, all candidates within a given $p_{\rm T}$ interval are identified as *trigger* particles. By selecting a trigger particle all remaining candidates within the same interval compose the group of *associated* particles. Particle pairs are then formed by combining every trigger particle with each associated particle. The two-particle correlation function is composed of a signal part $S(\Delta\eta, \Delta\phi)$, a background part $B(\Delta\eta, \Delta\phi)$, and a normalization factor $B(0, 0)$. The total function is defined as the associated yield per trigger particle, given by

$$\frac{1}{N_{\rm trig}} \frac{\mathrm{d}^2 N_{\rm pair}}{\mathrm{d}\Delta\eta\,\mathrm{d}\Delta\phi} = \frac{S(\Delta\eta, \Delta\phi)}{B(\Delta\eta, \Delta\phi)} \times B(0, 0), \tag{2}$$

where $N_{\rm pair}$ is the number of particle pairs found in a $(\Delta\eta, \Delta\phi)$ bin. The number of trigger particles within a given $p_{\rm T}$ interval and activity class is denoted by $N_{\rm trig}$. The signal

distribution $S(\Delta\eta, \Delta\phi)$ describes the associated yield per trigger particle for particle pairs, N_{same}, formed from the same event, and is defined as

$$S(\Delta\eta, \Delta\phi) = \frac{1}{N_{\text{trig}}} \frac{\mathrm{d}^2 N_{\text{same}}}{\mathrm{d}\Delta\eta\, \mathrm{d}\Delta\phi}. \tag{3}$$

Following the approach in Ref. [4], the sum over the events is performed separately for N_{trig} and for $\mathrm{d}^2 N_{\text{same}}/\mathrm{d}\Delta\eta\, \mathrm{d}\Delta\phi$ before the ratio is calculated. The background distribution $B(\Delta\eta, \Delta\phi)$ is defined for particle pairs of mixed events,

$$B(\Delta\eta, \Delta\phi) = \frac{\mathrm{d}^2 N_{\text{mix}}}{\mathrm{d}\Delta\eta\, \mathrm{d}\Delta\phi}, \tag{4}$$

and describes the yield of uncorrelated particles. The N_{mix} pairs are constructed by combining all trigger particles of an event with the associated particles of five different random events in the same activity class, whose vertex positions in the beam direction are within 2 cm of the original event. As a result, effects due to the detector occupancy, acceptance and material are accounted for by dividing the signal by the background distribution, where the latter is normalised to unity around the origin. The factor $B(0, 0)$ describes the associated yield for particles of a pair travelling in approximately the same direction and thus having the maximum pair acceptance.

All trigger and associated particles in the signal and background distributions are weighted with the correction factors ω described in Section 3. Furthermore, alternative correction factors determined from the large pile-up pp simulation using Pythia are applied to evaluate systematic uncertainties. The resulting associated correlation yields agree within 3% with the nominal results. To estimate the influence of the track selection, the correction factors are also determined with a maximum impact parameter relaxed to twice the nominal value, and the value of the multivariate classifier used to suppress fake tracks is varied by ±5%. The resulting different correction factors are applied to the measurements which are then compared to the nominal corrected results. The difference due to the different prompt selection is negligible, while the alternative fake track suppression results in a maximum variation of 3%.

6 Results

Two-particle correlation functions for events recorded in the p+Pb configuration are presented in Fig. 2. The correlation for particles with $1 < p_{\text{T}} < 2\,\text{GeV}/c$ is shown for events of the $50 - 100\%$ and $0 - 3\%$ class, representing low and very-high event activities, respectively. Both histograms are dominated by the jet peak around $\Delta\eta \approx \Delta\phi \approx 0$ which is due to correlations of particles originating from the same jet-like objects and thus being boosted closely together. To have a better visualization of additional structures the jet peak is truncated in all 2D-histograms. The second prominent feature is visible on the away-side ($\Delta\phi \approx \pi$) over a long range in $\Delta\eta$. The event sample with very high event activity (Fig. 2, right) shows an additional, less pronounced, long-range structure centred

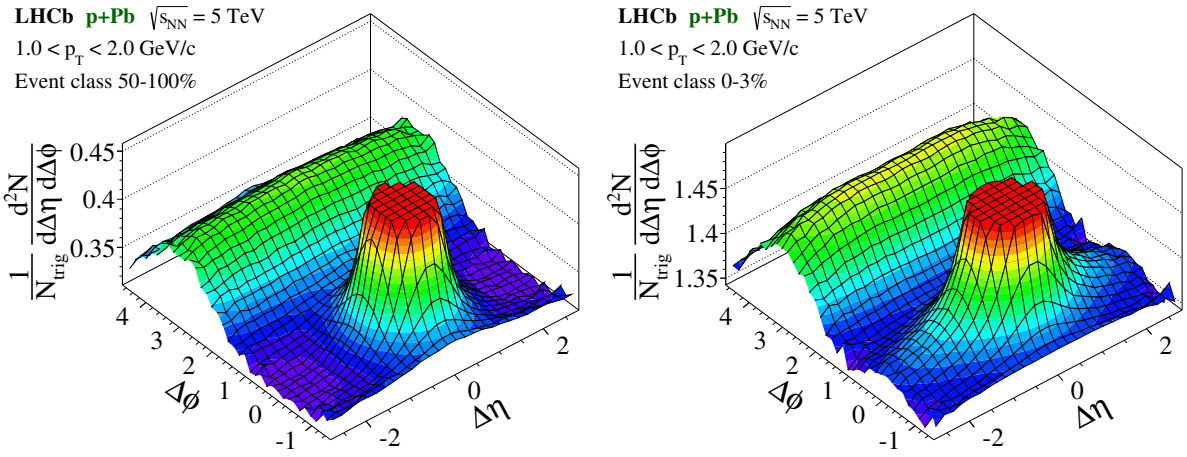

Figure 2: Two-particle correlation functions for events recorded in the p+Pb configuration, showing the (left) low and (right) high event-activity classes. The analysed pairs of prompt charged particles are selected in a p_{T} range of $1-2\,\mathrm{GeV}/c$. The near-side peak around $\Delta\eta = \Delta\phi = 0$ is truncated in the histograms.

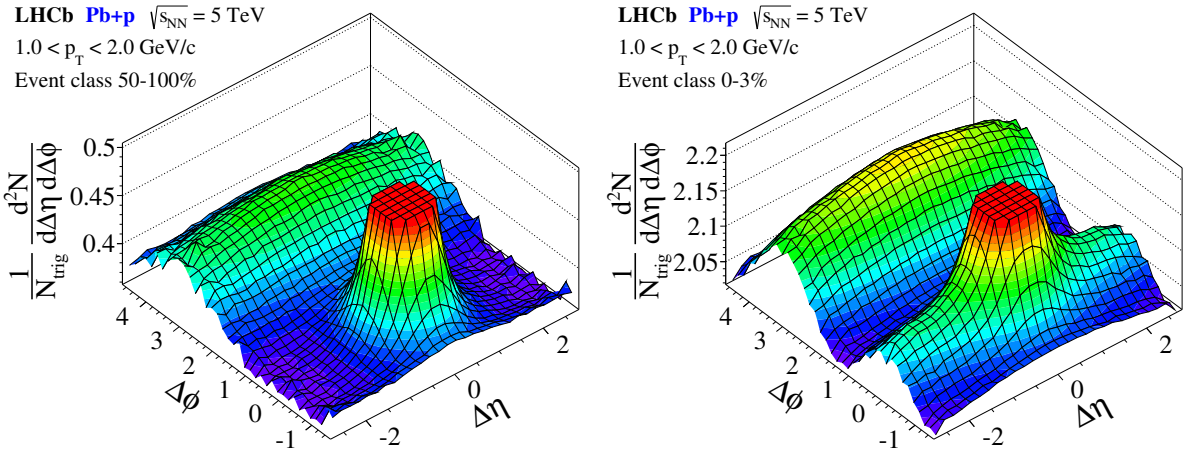

Figure 3: Two-particle correlation functions for events recorded in the Pb+p configuration, showing the (left) low and (right) high event-activity classes. The analysed pairs of prompt charged particles are selected in a p_{T} range of $1-2\,\mathrm{GeV}/c$. The near-side peak around $(\Delta\eta = \Delta\phi = 0)$ is truncated in the histograms.

at $\Delta\phi = 0$, which is not present in the corresponding low-activity sample. The structure, often referred to as the near-side ridge, is elongated over the full measured $\Delta\eta$ range of 2.9 units. This observation of the ridge for particles produced in proton-lead collisions at forward rapidities, $2.0 < \eta < 4.9$, extends previous central rapidity measurements at the LHC.

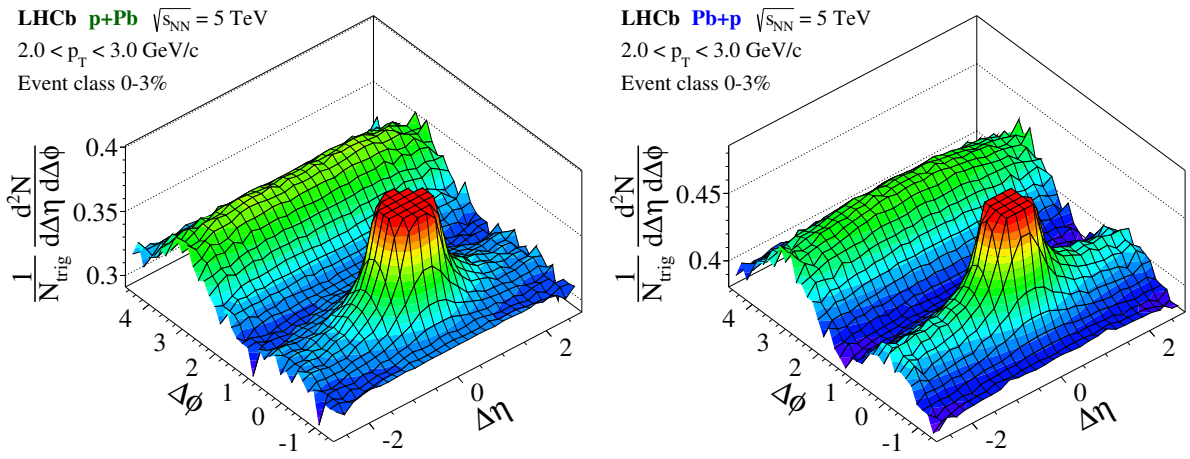

Figure 4: Two-particle correlation functions for events recorded in the p+Pb (left) and Pb+p (right) configurations, showing the $0-3\%$ event-activity class. The analysed pairs of prompt charged particles are selected in a p_{T} range of $2-3\,\mathrm{GeV}/c$. The near-side peak around ($\Delta\eta = \Delta\phi = 0$) is truncated in each histogram.

Two-particle correlations for events recorded in the Pb+p configuration are shown in Fig. 3, again for particle pairs with $1 < p_{\mathrm{T}} < 2\,\mathrm{GeV}/c$. The $50-100\%$ and $0-3\%$ activity classes in the Pb+p sample exhibit the same correlation structures as the corresponding classes in the p+Pb sample. While the shape and magnitude of the jet peak and the away-side ridge appear to be of similar sizes in both beam configurations, the near-side ridge is more pronounced for particles in the direction of the lead beam. For the 3% of events with the highest event activity, the near-side ridge in the Pb+p sample is much more prominent than that in the p+Pb sample.

Similar behaviour is found when analysing particle pairs with larger transverse momenta in the interval $2 < p_{\mathrm{T}} < 3\,\mathrm{GeV}/c$. In Fig. 4 the correlation functions in this p_{T} range are presented for the 3% highest-activity events recorded in the p+Pb and Pb+p configurations. The near-side ridge is present in both samples; however in the p+Pb sample it is only marginally visible while in the Pb+p sample a strongly pronounced ridge is found. The short-range jet peak in this higher p_{T} interval is more collimated compared to the $1-2\,\mathrm{GeV}/c$ interval, because of the higher average total momentum of the particles. As a result, the near-side ridge is visible towards $|\Delta\eta|$ values slightly below 2.0 without being covered by the jet peak.

In order to study the evolution of the long-range correlations on the near and away sides in more detail, one-dimensional projections of the correlation function on $\Delta\phi$ are calculated,

$$Y(\Delta\phi) \equiv \frac{1}{N_{\mathrm{trig}}}\frac{\mathrm{d}N_{\mathrm{pair}}}{\mathrm{d}\Delta\phi} = \frac{1}{\Delta\eta_b - \Delta\eta_a}\int_{\Delta\eta_a}^{\Delta\eta_b}\frac{1}{N_{\mathrm{trig}}}\frac{\mathrm{d}^2N_{\mathrm{pair}}}{\mathrm{d}\Delta\eta\mathrm{d}\Delta\phi}\mathrm{d}\Delta\eta. \tag{5}$$

The short-range correlations, *e.g.* of the jet-peak, are excluded by averaging the two-

dimensional yield over the interval from $\Delta\eta_a = 2.0$ to $\Delta\eta_b = 2.9$. Since multiple sources of correlations produce a flat pedestal in the yield, the correlation structures of interest are extracted by using the zero-yield-at-minimum (ZYAM) method [30]. By fitting a second-order polynomial to $Y(\Delta\phi)$ in the range $0.1 < \Delta\phi < 2.0$, the offset is estimated as the minimum of the polynomial. This value, further denoted as C_{ZYAM}, is subtracted from $Y(\Delta\phi)$ to shift its minimum to be at zero yield. The uncertainties on C_{ZYAM} due to the limited sample size and the fit range are below 0.002 for all individual measurements.

The subtracted one-dimensional yields for the p+Pb (full circles) and Pb+p (open circles) data samples are shown in Fig. 5 for all activity classes and p_{T} intervals. The correlation strength increases with event activity, but decreases towards higher p_{T} where fewer particles are found. Since more particles are emitted into the acceptance of the detector in the Pb+p compared to the p+Pb configuration, a larger offset is observed, as indicated by the ZYAM constants. All distributions in Fig. 5 show a maximum at $\Delta\phi = \pi$, marking the centre of the away-side ridge, which balances the momentum of the near-side (the jet peak is excluded in this representation). The lower activity classes, $50 - 100\%$ and $30 - 50\%$, do not have a corresponding maximum at $\Delta\phi = 0$. The $30 - 50\%$ event class of the Pb+p sample shows a first change in shape of the distribution at $\Delta\phi = 0$. The picture changes when probing the intermediate activity class $10 - 30\%$. In all p_{T} intervals of the Pb+p sample the emergence of the near-side ridge with a second maximum at $\Delta\phi = 0$ is clearly visible. In the p+Pb sample the event activity is still not high enough to form a clear near-side structure. In the high-activity classes, $0 - 10\%$ and $0 - 3\%$, the near-side ridge is strongly pronounced in the Pb+p sample in all p_{T} intervals. In the p+Pb sample the near-side structure is less distinct; however the $1 < p_{\mathrm{T}} < 2\,\mathrm{GeV}/c$ interval shows a clear near-side ridge.

Comparison of the ZYAM-subtracted yields within an activity class for different p_{T} intervals shows that the maximum of the away-side ridge decreases monotonically towards higher p_{T}, while the near-side ridge, if present, has its maximum in the range $1 < p_{\mathrm{T}} < 2\,\mathrm{GeV}/c$. The ratio between the subtracted yields on the near and away sides exceeds more than 50% in the $0 - 3\%$ activity classes of the Pb+p sample; in the p+Pb sample the ratio is still larger than 25%.

Study of the one-dimensional yields within a p_{T} interval for different activity classes shows that the away side remains approximately unchanged, while the near side starts to form the additional ridge when a certain event activity is reached. This turn-on, however, appears to be at different activities in the p+Pb and Pb+p configurations.

The same qualitative observations in the various analysis bins, including the emergence of the near-side ridge, are found when using the track-based approach for the definition of the activity classes as a systematic check. The total correlation yield varies by a few percent and does not exceed the maximum variation of 10% in the low-p_{T} range. The emergence of the near-side ridge in the ZYAM-subtracted yield is unaffected by the change of the event activity definition.

Further systematic effects related to the event selection are evaluated by including events with multiple reconstructed primary vertices. The change of the final correlation yield is negligible. As another cross-check, data recorded in magnet up and down polarities

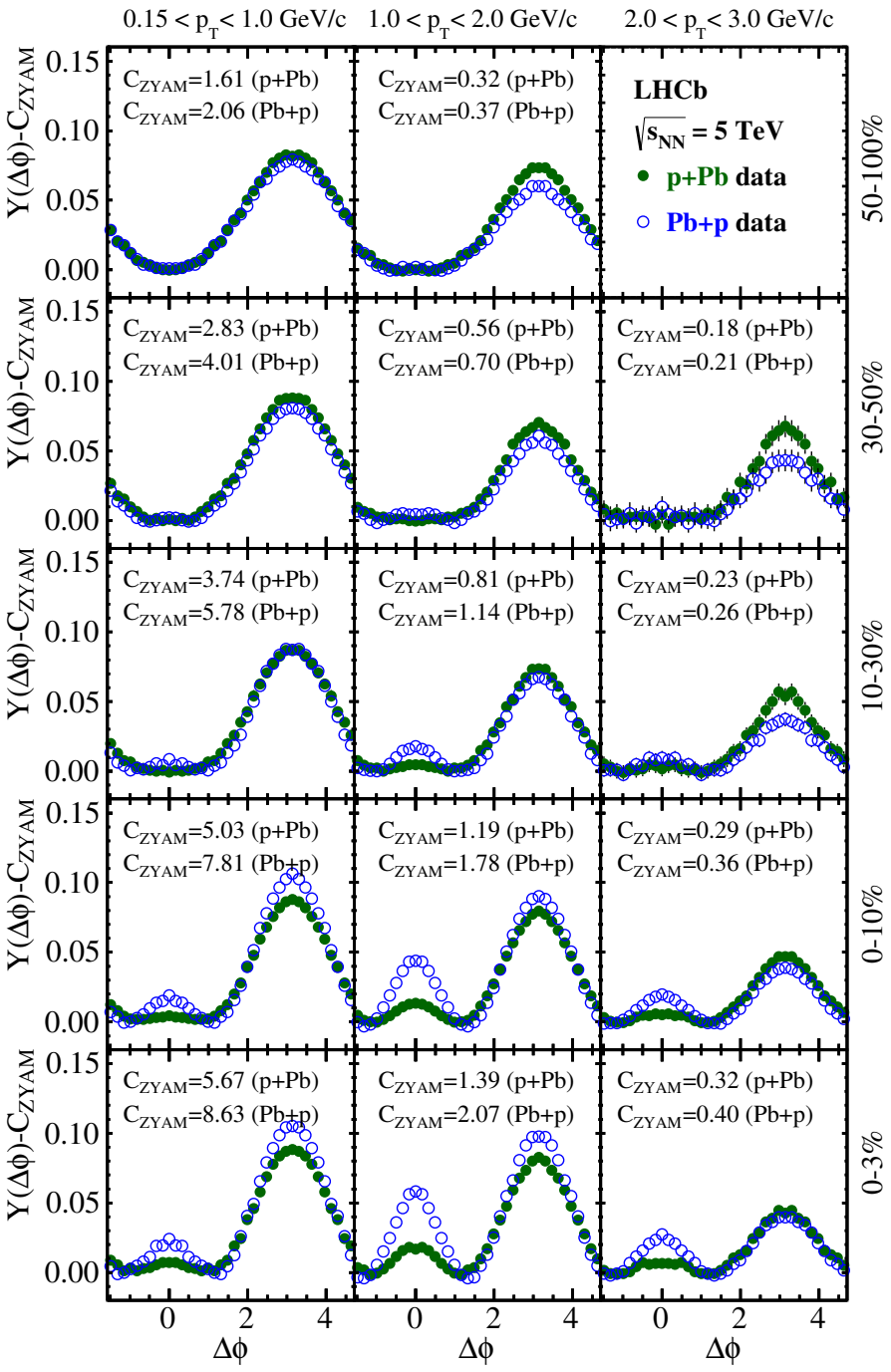

Figure 5: One-dimensional correlation yield as a function of $\Delta\phi$ obtained from the ZYAM-method by averaging over $2.0 < \Delta\eta < 2.9$. The subtracted yields are presented for $\sqrt{s_{NN}} = 5\,\text{TeV}$ proton-lead collisions recorded in p+Pb (full green circles) and Pb+p (open blue circles) configurations. The ZYAM constant is given in each panel. Event classes are compared for low to very-high activities from top to bottom, and different intervals of increasing p_T from left to right. Only statistical uncertainties are shown. Error bars are often smaller than the markers.

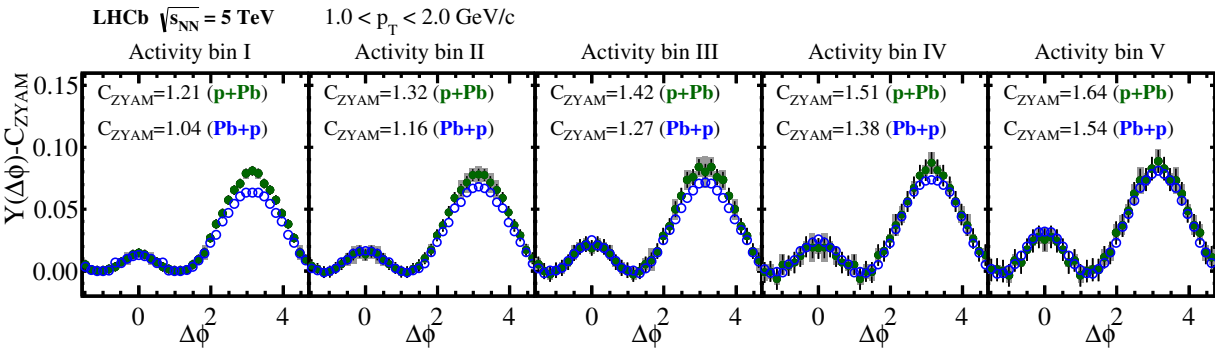

Figure 6: One-dimensional correlation yield as a function of $\Delta\phi$ obtained from the ZYAM-method by averaging the two-dimensional distribution over $2.0 < \Delta\eta < 2.9$. The results for the p+Pb and Pb+p samples are compared in five event classes which probe identical activities in the range $2.0 < \eta < 4.9$. The measured hit-multiplicities of the p+Pb sample are scaled to agree with the hit-multiplicities of the Pb+p sample. The uncertainty band represents the systematic limitation of the scaling procedure. The error bars represent the statistical uncertainty.

are analysed separately. The results are in good agreement with each other.

To investigate the activity dependence of the long-range correlations in the p+Pb and Pb+p samples in more detail, common bins in absolute activity for both samples are studied. For this purpose, events of both samples are probed in which a similar number of charged particles are emitted into the forward direction. Events of both samples are grouped into five narrow activity bins, as defined in Table 2. Figure 6 compares the ZYAM-subtracted two-particle correlation yields in the range $1 < p_{\mathrm{T}} < 2\,\mathrm{GeV}/c$, in which the near-side ridge is most pronounced. The uncertainty bands represent the systematic uncertainty on the scaling factor, which translates the activity of the p+Pb configuration to that of the Pb+p configuration. For p+Pb and Pb+p events of the same activity in the forward region, the observed long-range correlations become compatible within the uncertainties, except for bin I in which the away-side yield in p+Pb is still slightly more pronounced. A consistent increase of the near- and the away-side correlation strengths with increasing event activity is found in both hemispheres of the proton-lead collisions. Both the away-side correlations and the near-side ridge appear to be independent of the beam (p) or the target (Pb) fragmentation, and only depend on the activity in the corresponding direction.

7 Summary and conclusions

Two-particle angular correlations between prompt charged particles produced in pPb collisions at $\sqrt{s_{NN}} = 5\,\mathrm{TeV}$ have been measured for the first time in the forward region, using the LHCb detector. The angular correlations are studied in the laboratory frame in the pseudorapidity range $2.0 < \eta < 4.9$ over the full range of azimuthal angles, probing particle pairs in different common p_{T} intervals. With the asymmetric detector

layout, the analysis is performed separately for the p+Pb and Pb+p beam configurations, which probe rapidities in the nucleon-nucleon centre-of-mass frame of $1.5 < y < 4.4$ and $-5.4 < y < -2.5$, respectively. The strength of the near-side ridge observed in the backward (Pb+p configuration) region appears to be of similar size to that found in the forward (p+Pb configuration) region. The relative shift of about one unit in nucleon-nucleon centre-of-mass rapidity between the two configurations produces no sizeable effect on the near-side ridge within the accuracy of the measurement. For events with high event activity a long-range correlation on the near side (the ridge) is observed in both configurations. While the correlation structure on the away side shrinks with increasing p_{T}, the near-side ridge is most pronounced in the range $1 < p_{\mathrm{T}} < 2\,\mathrm{GeV}/c$. The observation of the ridge in the forward region extends LHC measurements performed at central rapidity, which show similar qualitative features. Furthermore, the correlation dependence on the event activity is investigated for relative and absolute activity ranges. The correlation structures on the near side and on the away side both grow stronger with increasing event activity. For identical absolute activity ranges in the p+Pb and Pb+p configurations the observed long-range correlations are compatible with each other.

Acknowledgements

We express our gratitude to our colleagues in the CERN accelerator departments for the excellent performance of the LHC. We thank the technical and administrative staff at the LHCb institutes. We acknowledge support from CERN and from the national agencies: CAPES, CNPq, FAPERJ and FINEP (Brazil); NSFC (China); CNRS/IN2P3 (France); BMBF, DFG and MPG (Germany); INFN (Italy); FOM and NWO (The Netherlands); MNiSW and NCN (Poland); MEN/IFA (Romania); MinES and FANO (Russia); MinECo (Spain); SNSF and SER (Switzerland); NASU (Ukraine); STFC (United Kingdom); NSF (USA). We acknowledge the computing resources that are provided by CERN, IN2P3 (France), KIT and DESY (Germany), INFN (Italy), SURF (The Netherlands), PIC (Spain), GridPP (United Kingdom), RRCKI (Russia), CSCS (Switzerland), IFIN-HH (Romania), CBPF (Brazil), PL-GRID (Poland) and OSC (USA). We are indebted to the communities behind the multiple open source software packages on which we depend. We are also thankful for the computing resources and the access to software R&D tools provided by Yandex LLC (Russia). Individual groups or members have received support from AvH Foundation (Germany), EPLANET, Marie Skłodowska-Curie Actions and ERC (European Union), Conseil Général de Haute-Savoie, Labex ENIGMASS and OCEVU, Région Auvergne (France), RFBR (Russia), GVA, XuntaGal and GENCAT (Spain), The Royal Society and Royal Commission for the Exhibition of 1851 (United Kingdom).

References

[1] J.-Y. Ollitrault, *Anisotropy as a signature of transverse collective flow*, Phys. Rev. **D46** (1992) 229.

[2] CMS collaboration, V. Khachatryan *et al.*, *Observation of long-range near-side angular correlations in proton-proton collisions at the LHC*, JHEP **1009** (2010) 091, arXiv:1009.4122.

[3] CMS collaboration, S. Chatrchyan *et al.*, *Observation of long-range near-side angular correlations in proton-lead collisions at the LHC*, Phys. Lett. **B718** (2013) 795, arXiv:1210.5482.

[4] ALICE collaboration, B. Abelev *et al.*, *Long-range angular correlations on the near and away side in p-Pb collisions at* $\sqrt{s_{NN}} = 5.02$ *TeV*, Phys. Lett. **B719** (2013) 29, arXiv:1212.2001.

[5] ATLAS collaboration, G. Aad *et al.*, *Observation of associated near-side and away-side long-range correlations in* $\sqrt{s_{NN}}$*=5.02 TeV proton-lead collisions with the ATLAS detector*, Phys. Rev. Lett. **110** (2013) 182302, arXiv:1212.5198.

[6] ATLAS collaboration, G. Aad *et al.*, *Measurement of long-range pseudorapidity correlations and azimuthal harmonics in* $\sqrt{s_{NN}} = 5.02$ *TeV proton-lead collisions with the ATLAS detector*, Phys. Rev. **C90** (2014) 044906, arXiv:1409.1792.

[7] ALICE collaboration, J. Adam *et al.*, *Forward-central two-particle correlations in p-Pb collisions at* $\sqrt{s_{\rm NN}}$ *= 5.02 TeV*, arXiv:1506.08032.

[8] K. Dusling and R. Venugopalan, *Evidence for BFKL and saturation dynamics from dihadron spectra at the LHC*, Phys. Rev. **D87** (2013) 051502, arXiv:1210.3890.

[9] K. Dusling and R. Venugopalan, *Explanation of systematics of CMS p+Pb high multiplicity di-hadron data at* $\sqrt{s}_{\rm NN} = 5.02$ *TeV*, Phys. Rev. **D87** (2013) 054014, arXiv:1211.3701.

[10] Y. V. Kovchegov and D. E. Wertepny, *Long-range rapidity correlations in heavy-light ion collisions*, Nucl. Phys. **A906** (2013) 50, arXiv:1212.1195.

[11] K. Dusling and R. Venugopalan, *Comparison of the color glass condensate to dihadron correlations in proton-proton and proton-nucleus collisions*, Phys. Rev. **D87** (2013) 094034, arXiv:1302.7018.

[12] A. Bzdak, B. Schenke, P. Tribedy, and R. Venugopalan, *Initial state geometry and the role of hydrodynamics in proton-proton, proton-nucleus and deuteron-nucleus collisions*, Phys. Rev. **C87** (2013) 064906, arXiv:1304.3403.

[13] S. Alderweireldt and P. Van Mechelen, *Obtaining the CMS ridge effect with multiparton interactions*, Proceedings of the 3rd International Workshop on Multiple Partonic Interactions at the LHC (MPI@LHC 2011) (2012) 33, arXiv:1203.2048.

[14] M. Strikman, *Transverse nucleon structure and multiparton interactions*, Acta Phys. Polon. **B42** (2011) 2607, arXiv:1112.3834.

[15] M. G. Ryskin, A. D. Martin, and V. A. Khoze, *Probes of multiparticle production at the LHC*, J. Phys. **G38** (2011) 085006, arXiv:1105.4987.

[16] R. C. Hwa and C. B. Yang, *Ridge formation induced by jets in pp collisions at 7 TeV*, Phys. Rev. **C83** (2011) 024911, arXiv:1011.0965.

[17] C.-Y. Wong, *Momentum Kick Model description of the ridge in $\Delta\phi$-$\Delta\eta$ correlation in pp collisions at 7 TeV*, Phys. Rev. **C84** (2011) 024901, arXiv:1105.5871.

[18] E. Avsar *et al.*, *Eccentricity and elliptic flow in proton-proton collisions from parton evolution*, Phys. Lett. **B702** (2011) 394, arXiv:1009.5643.

[19] K. Werner, I. Karpenko, and T. Pierog, *The 'ridge' in proton-proton scattering at 7 TeV*, Phys. Rev. Lett. **106** (2011) 122004, arXiv:1011.0375.

[20] P. Bozek and W. Broniowski, *Correlations from hydrodynamic flow in p-Pb collisions*, Phys. Lett. **B718** (2013) 1557, arXiv:1211.0845.

[21] E. Shuryak and I. Zahed, *High-multiplicity pp and pA collisions: Hydrodynamics at its edge*, Phys. Rev. **C88** (2013) 044915, arXiv:1301.4470.

[22] LHCb collaboration, A. A. Alves Jr. *et al.*, *The LHCb detector at the LHC*, JINST **3** (2008) S08005.

[23] LHCb collaboration, R. Aaij *et al.*, *LHCb detector performance*, Int. J. Mod. Phys. **A30** (2015) 1530022, arXiv:1412.6352.

[24] X.-N. Wang and M. Gyulassy, *HIJING: A Monte Carlo model for multiple jet production in pp, pA and AA collisions*, Phys. Rev. **D44** (1991) 3501.

[25] T. Sjöstrand, S. Mrenna, and P. Skands, *A brief introduction to PYTHIA 8.1*, Comput. Phys. Commun. **178** (2008) 852, arXiv:0710.3820; T. Sjöstrand, S. Mrenna, and P. Skands, *PYTHIA 6.4 physics and manual*, JHEP **05** (2006) 026, arXiv:hep-ph/0603175.

[26] I. Belyaev *et al.*, *Handling of the generation of primary events in Gauss, the LHCb simulation framework*, J. Phys. Conf. Ser. **331** (2011) 032047.

[27] D. J. Lange, *The EvtGen particle decay simulation package*, Nucl. Instrum. Meth. **A462** (2001) 152.

[28] Geant4 collaboration, J. Allison *et al.*, *Geant4 developments and applications*, IEEE Trans. Nucl. Sci. **53** (2006) 270; Geant4 collaboration, S. Agostinelli *et al.*, *Geant4: A simulation toolkit*, Nucl. Instrum. Meth. **A506** (2003) 250.

[29] M. Clemencic *et al.*, *The LHCb simulation application, Gauss: Design, evolution and experience*, J. Phys. Conf. Ser. **331** (2011) 032023.

[30] N. N. Ajitanand *et al.*, *Decomposition of harmonic and jet contributions to particle-pair correlations at ultrarelativistic energies*, Phys. Rev. C **72** (2005) 011902.

LHCb collaboration

R. Aaij[39], C. Abellán Beteta[41], B. Adeva[38], M. Adinolfi[47], A. Affolder[53], Z. Ajaltouni[5], S. Akar[6], J. Albrecht[10], F. Alessio[39], M. Alexander[52], S. Ali[42], G. Alkhazov[31], P. Alvarez Cartelle[54], A.A. Alves Jr[58], S. Amato[2], S. Amerio[23], Y. Amhis[7], L. An[3], L. Anderlini[18], J. Anderson[41], G. Andreassi[40], M. Andreotti[17,f], J.E. Andrews[59], R.B. Appleby[55], O. Aquines Gutierrez[11], F. Archilli[39], P. d'Argent[12], A. Artamonov[36], M. Artuso[60], E. Aslanides[6], G. Auriemma[26,m], M. Baalouch[5], S. Bachmann[12], J.J. Back[49], A. Badalov[37], C. Baesso[61], W. Baldini[17,39], R.J. Barlow[55], C. Barschel[39], S. Barsuk[7], W. Barter[39], V. Batozskaya[29], V. Battista[40], A. Bay[40], L. Beaucourt[4], J. Beddow[52], F. Bedeschi[24], I. Bediaga[1], L.J. Bel[42], V. Bellee[40], N. Belloli[21,j], I. Belyaev[32], E. Ben-Haim[8], G. Bencivenni[19], S. Benson[39], J. Benton[47], A. Berezhnoy[33], R. Bernet[41], A. Bertolin[23], M.-O. Bettler[39], M. van Beuzekom[42], A. Bien[12], S. Bifani[46], P. Billoir[8], T. Bird[55], A. Birnkraut[10], A. Bizzeti[18,h], T. Blake[49], F. Blanc[40], J. Blouw[11], S. Blusk[60], V. Bocci[26], A. Bondar[35], N. Bondar[31,39], W. Bonivento[16], S. Borghi[55], M. Borsato[7], T.J.V. Bowcock[53], E. Bowen[41], C. Bozzi[17], S. Braun[12], M. Britsch[11], T. Britton[60], J. Brodzicka[55], N.H. Brook[47], E. Buchanan[47], C. Burr[55], A. Bursche[41], J. Buytaert[39], S. Cadeddu[16], R. Calabrese[17,f], M. Calvi[21,j], M. Calvo Gomez[37,o], P. Campana[19], D. Campora Perez[39], L. Capriotti[55], A. Carbone[15,d], G. Carboni[25,k], R. Cardinale[20,i], A. Cardini[16], P. Carniti[21,j], L. Carson[51], K. Carvalho Akiba[2,39], G. Casse[53], L. Cassina[21,j], L. Castillo Garcia[40], M. Cattaneo[39], Ch. Cauet[10], G. Cavallero[20], R. Cenci[24,s], M. Charles[8], Ph. Charpentier[39], M. Chefdeville[4], S. Chen[55], S.-F. Cheung[56], N. Chiapolini[41], M. Chrzaszcz[41], X. Cid Vidal[39], G. Ciezarek[42], P.E.L. Clarke[51], M. Clemencic[39], H.V. Cliff[48], J. Closier[39], V. Coco[39], J. Cogan[6], E. Cogneras[5], V. Cogoni[16,e], L. Cojocariu[30], G. Collazuol[23,q], P. Collins[39], A. Comerma-Montells[12], A. Contu[16], A. Cook[47], M. Coombes[47], S. Coquereau[8], G. Corti[39], M. Corvo[17,f], B. Couturier[39], G.A. Cowan[51], D.C. Craik[49], A. Crocombe[49], M. Cruz Torres[61], S. Cunliffe[54], R. Currie[54], C. D'Ambrosio[39], E. Dall'Occo[42], J. Dalseno[47], P.N.Y. David[42], A. Davis[58], O. De Aguiar Francisco[2], K. De Bruyn[6], S. De Capua[55], M. De Cian[12], J.M. De Miranda[1], L. De Paula[2], P. De Simone[19], C.-T. Dean[52], D. Decamp[4], M. Deckenhoff[10], L. Del Buono[8], N. Déléage[4], M. Demmer[10], D. Derkach[66], O. Deschamps[5], F. Dettori[39], B. Dey[22], A. Di Canto[39], F. Di Ruscio[25], H. Dijkstra[39], S. Donleavy[53], F. Dordei[12], M. Dorigo[40], A. Dosil Suárez[38], D. Dossett[49], A. Dovbnya[44], K. Dreimanis[53], L. Dufour[42], G. Dujany[55], F. Dupertuis[40], P. Durante[39], R. Dzhelyadin[36], A. Dziurda[27], A. Dzyuba[31], S. Easo[50,39], U. Egede[54], V. Egorychev[32], S. Eidelman[35], S. Eisenhardt[51], U. Eitschberger[10], R. Ekelhof[10], L. Eklund[52], I. El Rifai[5], Ch. Elsasser[41], S. Ely[60], S. Esen[12], H.M. Evans[48], T. Evans[56], A. Falabella[15], C. Färber[39], N. Farley[46], S. Farry[53], R. Fay[53], D. Ferguson[51], V. Fernandez Albor[38], F. Ferrari[15], F. Ferreira Rodrigues[1], M. Ferro-Luzzi[39], S. Filippov[34], M. Fiore[17,39,f], M. Fiorini[17,f], M. Firlej[28], C. Fitzpatrick[40], T. Fiutowski[28], K. Fohl[39], P. Fol[54], M. Fontana[16], F. Fontanelli[20,i], D. C. Forshaw[60], R. Forty[39], M. Frank[39], C. Frei[39], M. Frosini[18], J. Fu[22], E. Furfaro[25,k], A. Gallas Torreira[38], D. Galli[15,d], S. Gallorini[23], S. Gambetta[51], M. Gandelman[2], P. Gandini[56], Y. Gao[3], J. García Pardiñas[38], J. Garra Tico[48], L. Garrido[37], D. Gascon[37], C. Gaspar[39], R. Gauld[56], L. Gavardi[10], G. Gazzoni[5], D. Gerick[12], E. Gersabeck[12], M. Gersabeck[55], T. Gershon[49], Ph. Ghez[4], S. Gianì[40], V. Gibson[48], O.G. Girard[40], L. Giubega[30], V.V. Gligorov[39], C. Göbel[61], D. Golubkov[32], A. Golutvin[54,39], A. Gomes[1,a], C. Gotti[21,j], M. Grabalosa Gándara[5], R. Graciani Diaz[37], L.A. Granado Cardoso[39], E. Graugés[37], E. Graverini[41], G. Graziani[18], A. Grecu[30], E. Greening[56], S. Gregson[48], P. Griffith[46], L. Grillo[12], O. Grünberg[64], B. Gui[60], E. Gushchin[34], Yu. Guz[36,39], T. Gys[39], T. Hadavizadeh[56],

C. Hadjivasiliou[60], G. Haefeli[40], C. Haen[39], S.C. Haines[48], S. Hall[54], B. Hamilton[59], X. Han[12], S. Hansmann-Menzemer[12], N. Harnew[56], S.T. Harnew[47], J. Harrison[55], J. He[39], T. Head[40], V. Heijne[42], A. Heister[9], K. Hennessy[53], P. Henrard[5], L. Henry[8], J.A. Hernando Morata[38], E. van Herwijnen[39], M. Heß[64], A. Hicheur[2], D. Hill[56], M. Hoballah[5], C. Hombach[55], W. Hulsbergen[42], T. Humair[54], N. Hussain[56], D. Hutchcroft[53], D. Hynds[52], M. Idzik[28], P. Ilten[57], R. Jacobsson[39], A. Jaeger[12], J. Jalocha[56], E. Jans[42], A. Jawahery[59], F. Jing[3], M. John[56], D. Johnson[39], C.R. Jones[48], C. Joram[39], B. Jost[39], N. Jurik[60], S. Kandybei[44], W. Kanso[6], M. Karacson[39], T.M. Karbach[39,†], S. Karodia[52], M. Kecke[12], M. Kelsey[60], I.R. Kenyon[46], M. Kenzie[39], T. Ketel[43], E. Khairullin[66], B. Khanji[21,39,j], C. Khurewathanakul[40], T. Kirn[9], S. Klaver[55], K. Klimaszewski[29], O. Kochebina[7], M. Kolpin[12], I. Komarov[40], R.F. Koopman[43], P. Koppenburg[42,39], M. Kozeiha[5], L. Kravchuk[34], K. Kreplin[12], M. Kreps[49], G. Krocker[12], P. Krokovny[35], F. Kruse[10], W. Krzemien[29], W. Kucewicz[27,n], M. Kucharczyk[27], V. Kudryavtsev[35], A. K. Kuonen[40], K. Kurek[29], T. Kvaratskheliya[32], D. Lacarrere[39], G. Lafferty[55,39], A. Lai[16], D. Lambert[51], G. Lanfranchi[19], C. Langenbruch[49], B. Langhans[39], T. Latham[49], C. Lazzeroni[46], R. Le Gac[6], J. van Leerdam[42], J.-P. Lees[4], R. Lefèvre[5], A. Leflat[33,39], J. Lefrançois[7], E. Lemos Cid[38], O. Leroy[6], T. Lesiak[27], B. Leverington[12], Y. Li[7], T. Likhomanenko[66,65], M. Liles[53], R. Lindner[39], C. Linn[39], F. Lionetto[41], B. Liu[16], X. Liu[3], D. Loh[49], I. Longstaff[52], J.H. Lopes[2], D. Lucchesi[23,q], M. Lucio Martinez[38], H. Luo[51], A. Lupato[23], E. Luppi[17,f], O. Lupton[56], A. Lusiani[24], F. Machefert[7], F. Maciuc[30], O. Maev[31], K. Maguire[55], S. Malde[56], A. Malinin[65], G. Manca[7], G. Mancinelli[6], P. Manning[60], A. Mapelli[39], J. Maratas[5], J.F. Marchand[4], U. Marconi[15], C. Marin Benito[37], P. Marino[24,39,s], J. Marks[12], G. Martellotti[26], M. Martin[6], M. Martinelli[40], D. Martinez Santos[38], F. Martinez Vidal[67], D. Martins Tostes[2], A. Massafferri[1], R. Matev[39], A. Mathad[49], Z. Mathe[39], C. Matteuzzi[21], A. Mauri[41], B. Maurin[40], A. Mazurov[46], M. McCann[54], J. McCarthy[46], A. McNab[55], R. McNulty[13], B. Meadows[58], F. Meier[10], M. Meissner[12], D. Melnychuk[29], M. Merk[42], E Michielin[23], D.A. Milanes[63], M.-N. Minard[4], D.S. Mitzel[12], J. Molina Rodriguez[61], I.A. Monroy[63], S. Monteil[5], M. Morandin[23], P. Morawski[28], A. Mordà[6], M.J. Morello[24,s], J. Moron[28], A.B. Morris[51], R. Mountain[60], F. Muheim[51], D. Müller[55], J. Müller[10], K. Müller[41], V. Müller[10], M. Mussini[15], B. Muster[40], P. Naik[47], T. Nakada[40], R. Nandakumar[50], A. Nandi[56], I. Nasteva[2], M. Needham[51], N. Neri[22], S. Neubert[12], N. Neufeld[39], M. Neuner[12], A.D. Nguyen[40], T.D. Nguyen[40], C. Nguyen-Mau[40,p], V. Niess[5], R. Niet[10], N. Nikitin[33], T. Nikodem[12], A. Novoselov[36], D.P. O'Hanlon[49], A. Oblakowska-Mucha[28], V. Obraztsov[36], S. Ogilvy[52], O. Okhrimenko[45], R. Oldeman[16,e], C.J.G. Onderwater[68], B. Osorio Rodrigues[1], J.M. Otalora Goicochea[2], A. Otto[39], P. Owen[54], A. Oyanguren[67], A. Palano[14,c], F. Palombo[22,t], M. Palutan[19], J. Panman[39], A. Papanestis[50], M. Pappagallo[52], L.L. Pappalardo[17,f], C. Pappenheimer[58], W. Parker[59], C. Parkes[55], G. Passaleva[18], G.D. Patel[53], M. Patel[54], C. Patrignani[20,i], A. Pearce[55,50], A. Pellegrino[42], G. Penso[26,l], M. Pepe Altarelli[39], S. Perazzini[15,d], P. Perret[5], L. Pescatore[46], K. Petridis[47], A. Petrolini[20,i], M. Petruzzo[22], E. Picatoste Olloqui[37], B. Pietrzyk[4], T. Pilař[49], D. Pinci[26], A. Pistone[20], A. Piucci[12], S. Playfer[51], M. Plo Casasus[38], T. Poikela[39], F. Polci[8], A. Poluektov[49,35], I. Polyakov[32], E. Polycarpo[2], A. Popov[36], D. Popov[11,39], B. Popovici[30], C. Potterat[2], E. Price[47], J.D. Price[53], J. Prisciandaro[38], A. Pritchard[53], C. Prouve[47], V. Pugatch[45], A. Puig Navarro[40], G. Punzi[24,r], W. Qian[4], R. Quagliani[7,47], B. Rachwal[27], J.H. Rademacker[47], M. Rama[24], M.S. Rangel[2], I. Raniuk[44], N. Rauschmayr[39], G. Raven[43], F. Redi[54], S. Reichert[55], M.M. Reid[49], A.C. dos Reis[1], S. Ricciardi[50], S. Richards[47], M. Rihl[39], K. Rinnert[53,39], V. Rives Molina[37], P. Robbe[7,39], A.B. Rodrigues[1], E. Rodrigues[55], J.A. Rodriguez Lopez[63], P. Rodriguez Perez[55],

S. Roiser[39], V. Romanovsky[36], A. Romero Vidal[38], J. W. Ronayne[13], M. Rotondo[23], J. Rouvinet[40], T. Ruf[39], P. Ruiz Valls[67], J.J. Saborido Silva[38], N. Sagidova[31], P. Sail[52], B. Saitta[16,e], V. Salustino Guimaraes[2], C. Sanchez Mayordomo[67], B. Sanmartin Sedes[38], R. Santacesaria[26], C. Santamarina Rios[38], M. Santimaria[19], E. Santovetti[25,k], A. Sarti[19,l], C. Satriano[26,m], A. Satta[25], D.M. Saunders[47], D. Savrina[32,33], S. Schael[9], M. Schiller[39], H. Schindler[39], M. Schlupp[10], M. Schmelling[11], T. Schmelzer[10], B. Schmidt[39], O. Schneider[40], A. Schopper[39], M. Schubiger[40], M.-H. Schune[7], R. Schwemmer[39], B. Sciascia[19], A. Sciubba[26,l], A. Semennikov[32], A. Sergi[46], N. Serra[41], J. Serrano[6], L. Sestini[23], P. Seyfert[21], M. Shapkin[36], I. Shapoval[17,44,f], Y. Shcheglov[31], T. Shears[53], L. Shekhtman[35], V. Shevchenko[65], A. Shires[10], B.G. Siddi[17], R. Silva Coutinho[41], L. Silva de Oliveira[2], G. Simi[23,r], M. Sirendi[48], N. Skidmore[47], T. Skwarnicki[60], E. Smith[56,50], E. Smith[54], I.T. Smith[51], J. Smith[48], M. Smith[55], H. Snoek[42], M.D. Sokoloff[58,39], F.J.P. Soler[52], F. Soomro[40], D. Souza[47], B. Souza De Paula[2], B. Spaan[10], P. Spradlin[52], S. Sridharan[39], F. Stagni[39], M. Stahl[12], S. Stahl[39], S. Stefkova[54], O. Steinkamp[41], O. Stenyakin[36], S. Stevenson[56], S. Stoica[30], S. Stone[60], B. Storaci[41], S. Stracka[24,s], M. Straticiuc[30], U. Straumann[41], L. Sun[58], W. Sutcliffe[54], K. Swientek[28], S. Swientek[10], V. Syropoulos[43], M. Szczekowski[29], T. Szumlak[28], S. T'Jampens[4], A. Tayduganov[6], T. Tekampe[10], M. Teklishyn[7], G. Tellarini[17,f], F. Teubert[39], C. Thomas[56], E. Thomas[39], J. van Tilburg[42], V. Tisserand[4], M. Tobin[40], J. Todd[58], S. Tolk[43], L. Tomassetti[17,f], D. Tonelli[39], S. Topp-Joergensen[56], N. Torr[56], E. Tournefier[4], S. Tourneur[40], K. Trabelsi[40], M.T. Tran[40], M. Tresch[41], A. Trisovic[39], A. Tsaregorodtsev[6], P. Tsopelas[42], N. Tuning[42,39], A. Ukleja[29], A. Ustyuzhanin[66,65], U. Uwer[12], C. Vacca[16,39,e], V. Vagnoni[15], G. Valenti[15], A. Vallier[7], R. Vazquez Gomez[19], P. Vazquez Regueiro[38], C. Vázquez Sierra[38], S. Vecchi[17], M. van Veghel[43], J.J. Velthuis[47], M. Veltri[18,g], G. Veneziano[40], M. Vesterinen[12], B. Viaud[7], D. Vieira[2], M. Vieites Diaz[38], X. Vilasis-Cardona[37,o], V. Volkov[33], A. Vollhardt[41], D. Volyanskyy[11], D. Voong[47], A. Vorobyev[31], V. Vorobyev[35], C. Voß[64], J.A. de Vries[42], R. Waldi[64], C. Wallace[49], R. Wallace[13], J. Walsh[24], S. Wandernoth[12], J. Wang[60], D.R. Ward[48], N.K. Watson[46], D. Websdale[54], A. Weiden[41], M. Whitehead[49], G. Wilkinson[56,39], M. Wilkinson[60], M. Williams[39], M.P. Williams[46], M. Williams[57], T. Williams[46], F.F. Wilson[50], J. Wimberley[59], J. Wishahi[10], W. Wislicki[29], M. Witek[27], G. Wormser[7], S.A. Wotton[48], S. Wright[48], K. Wyllie[39], Y. Xie[62], Z. Xu[40], Z. Yang[3], J. Yu[62], X. Yuan[35], O. Yushchenko[36], M. Zangoli[15], M. Zavertyaev[11,b], L. Zhang[3], Y. Zhang[3], A. Zhelezov[12], A. Zhokhov[32], L. Zhong[3], V. Zhukov[9], S. Zucchelli[15].

[1] *Centro Brasileiro de Pesquisas Físicas (CBPF), Rio de Janeiro, Brazil*
[2] *Universidade Federal do Rio de Janeiro (UFRJ), Rio de Janeiro, Brazil*
[3] *Center for High Energy Physics, Tsinghua University, Beijing, China*
[4] *LAPP, Université Savoie Mont-Blanc, CNRS/IN2P3, Annecy-Le-Vieux, France*
[5] *Clermont Université, Université Blaise Pascal, CNRS/IN2P3, LPC, Clermont-Ferrand, France*
[6] *CPPM, Aix-Marseille Université, CNRS/IN2P3, Marseille, France*
[7] *LAL, Université Paris-Sud, CNRS/IN2P3, Orsay, France*
[8] *LPNHE, Université Pierre et Marie Curie, Université Paris Diderot, CNRS/IN2P3, Paris, France*
[9] *I. Physikalisches Institut, RWTH Aachen University, Aachen, Germany*
[10] *Fakultät Physik, Technische Universität Dortmund, Dortmund, Germany*
[11] *Max-Planck-Institut für Kernphysik (MPIK), Heidelberg, Germany*
[12] *Physikalisches Institut, Ruprecht-Karls-Universität Heidelberg, Heidelberg, Germany*
[13] *School of Physics, University College Dublin, Dublin, Ireland*
[14] *Sezione INFN di Bari, Bari, Italy*
[15] *Sezione INFN di Bologna, Bologna, Italy*

[16] *Sezione INFN di Cagliari, Cagliari, Italy*
[17] *Sezione INFN di Ferrara, Ferrara, Italy*
[18] *Sezione INFN di Firenze, Firenze, Italy*
[19] *Laboratori Nazionali dell'INFN di Frascati, Frascati, Italy*
[20] *Sezione INFN di Genova, Genova, Italy*
[21] *Sezione INFN di Milano Bicocca, Milano, Italy*
[22] *Sezione INFN di Milano, Milano, Italy*
[23] *Sezione INFN di Padova, Padova, Italy*
[24] *Sezione INFN di Pisa, Pisa, Italy*
[25] *Sezione INFN di Roma Tor Vergata, Roma, Italy*
[26] *Sezione INFN di Roma La Sapienza, Roma, Italy*
[27] *Henryk Niewodniczanski Institute of Nuclear Physics Polish Academy of Sciences, Kraków, Poland*
[28] *AGH - University of Science and Technology, Faculty of Physics and Applied Computer Science, Kraków, Poland*
[29] *National Center for Nuclear Research (NCBJ), Warsaw, Poland*
[30] *Horia Hulubei National Institute of Physics and Nuclear Engineering, Bucharest-Magurele, Romania*
[31] *Petersburg Nuclear Physics Institute (PNPI), Gatchina, Russia*
[32] *Institute of Theoretical and Experimental Physics (ITEP), Moscow, Russia*
[33] *Institute of Nuclear Physics, Moscow State University (SINP MSU), Moscow, Russia*
[34] *Institute for Nuclear Research of the Russian Academy of Sciences (INR RAN), Moscow, Russia*
[35] *Budker Institute of Nuclear Physics (SB RAS) and Novosibirsk State University, Novosibirsk, Russia*
[36] *Institute for High Energy Physics (IHEP), Protvino, Russia*
[37] *Universitat de Barcelona, Barcelona, Spain*
[38] *Universidad de Santiago de Compostela, Santiago de Compostela, Spain*
[39] *European Organization for Nuclear Research (CERN), Geneva, Switzerland*
[40] *Ecole Polytechnique Fédérale de Lausanne (EPFL), Lausanne, Switzerland*
[41] *Physik-Institut, Universität Zürich, Zürich, Switzerland*
[42] *Nikhef National Institute for Subatomic Physics, Amsterdam, The Netherlands*
[43] *Nikhef National Institute for Subatomic Physics and VU University Amsterdam, Amsterdam, The Netherlands*
[44] *NSC Kharkiv Institute of Physics and Technology (NSC KIPT), Kharkiv, Ukraine*
[45] *Institute for Nuclear Research of the National Academy of Sciences (KINR), Kyiv, Ukraine*
[46] *University of Birmingham, Birmingham, United Kingdom*
[47] *H.H. Wills Physics Laboratory, University of Bristol, Bristol, United Kingdom*
[48] *Cavendish Laboratory, University of Cambridge, Cambridge, United Kingdom*
[49] *Department of Physics, University of Warwick, Coventry, United Kingdom*
[50] *STFC Rutherford Appleton Laboratory, Didcot, United Kingdom*
[51] *School of Physics and Astronomy, University of Edinburgh, Edinburgh, United Kingdom*
[52] *School of Physics and Astronomy, University of Glasgow, Glasgow, United Kingdom*
[53] *Oliver Lodge Laboratory, University of Liverpool, Liverpool, United Kingdom*
[54] *Imperial College London, London, United Kingdom*
[55] *School of Physics and Astronomy, University of Manchester, Manchester, United Kingdom*
[56] *Department of Physics, University of Oxford, Oxford, United Kingdom*
[57] *Massachusetts Institute of Technology, Cambridge, MA, United States*
[58] *University of Cincinnati, Cincinnati, OH, United States*
[59] *University of Maryland, College Park, MD, United States*
[60] *Syracuse University, Syracuse, NY, United States*
[61] *Pontifícia Universidade Católica do Rio de Janeiro (PUC-Rio), Rio de Janeiro, Brazil, associated to* [2]
[62] *Institute of Particle Physics, Central China Normal University, Wuhan, Hubei, China, associated to* [3]
[63] *Departamento de Fisica , Universidad Nacional de Colombia, Bogota, Colombia, associated to* [8]
[64] *Institut für Physik, Universität Rostock, Rostock, Germany, associated to* [12]
[65] *National Research Centre Kurchatov Institute, Moscow, Russia, associated to* [32]

[66] *Yandex School of Data Analysis, Moscow, Russia, associated to* [32]
[67] *Instituto de Fisica Corpuscular (IFIC), Universitat de Valencia-CSIC, Valencia, Spain, associated to* [37]
[68] *Van Swinderen Institute, University of Groningen, Groningen, The Netherlands, associated to* [42]

[a] *Universidade Federal do Triângulo Mineiro (UFTM), Uberaba-MG, Brazil*
[b] *P.N. Lebedev Physical Institute, Russian Academy of Science (LPI RAS), Moscow, Russia*
[c] *Università di Bari, Bari, Italy*
[d] *Università di Bologna, Bologna, Italy*
[e] *Università di Cagliari, Cagliari, Italy*
[f] *Università di Ferrara, Ferrara, Italy*
[g] *Università di Urbino, Urbino, Italy*
[h] *Università di Modena e Reggio Emilia, Modena, Italy*
[i] *Università di Genova, Genova, Italy*
[j] *Università di Milano Bicocca, Milano, Italy*
[k] *Università di Roma Tor Vergata, Roma, Italy*
[l] *Università di Roma La Sapienza, Roma, Italy*
[m] *Università della Basilicata, Potenza, Italy*
[n] *AGH - University of Science and Technology, Faculty of Computer Science, Electronics and Telecommunications, Kraków, Poland*
[o] *LIFAELS, La Salle, Universitat Ramon Llull, Barcelona, Spain*
[p] *Hanoi University of Science, Hanoi, Viet Nam*
[q] *Università di Padova, Padova, Italy*
[r] *Università di Pisa, Pisa, Italy*
[s] *Scuola Normale Superiore, Pisa, Italy*
[t] *Università degli Studi di Milano, Milano, Italy*

[†] *Deceased*